TECHNICAL NOTE

Polarization-resolved Microscopy and Spectroscopy Solutions

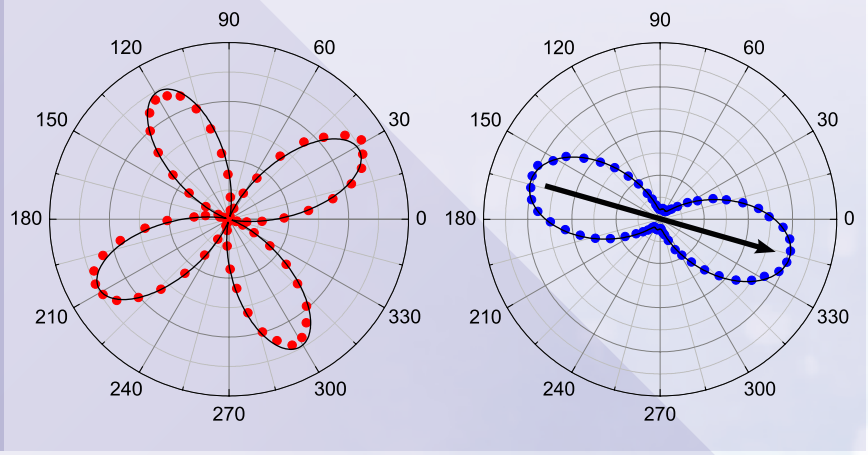

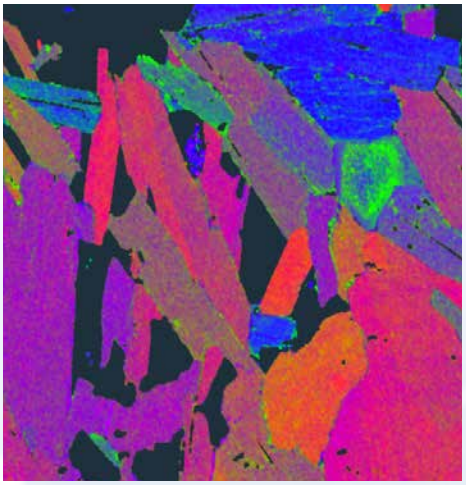

This Technical Note highlights Oxford Instruments WITec's Raman imaging microscopy and spectroscopy solutions for exploring polarization-dependent effects.

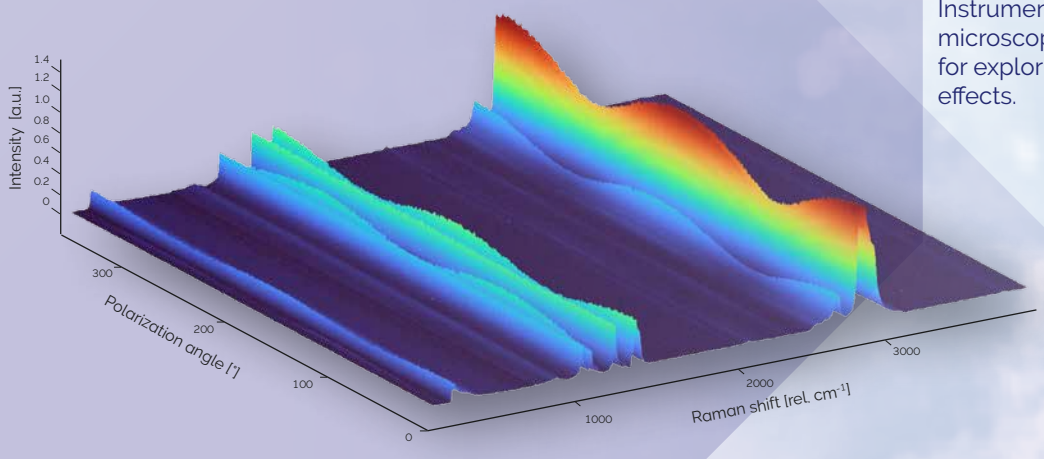

Polarization-resolved spectroscopy and microscopy

Polarization is a property of light that can be exploited with various microscopy techniques to obtain valuable insights into a sample's characteristics, including its structural orientation, optical anisotropy and chirality.

Polarized **white light microscopy** is widely used in geosciences to analyze the composition and optical properties of crystalline minerals. Further applications include the quantification and structural analysis of organic specimens, polymers and fibers.

Polarization-dependent **second-harmonic generation (SHG)** measurements are a powerful approach for characterizing crystal orientation and strain fields in samples such as 2D atomic crystals, which are of great interest to the semiconductor industry (for further information, see the WITec application note on Correlative Imaging of MoS_2 [1]).

Polarization-resolved **photoluminescence spectroscopy (PL)** reveals detailed information on electronic band structure and exciton dynamics in semiconducting materials.

In **Raman spectroscopy**, precise control of the polarization of both the excitation and scattered light offers an effective means for determining the symmetry and directionality of vibrational modes. In highly ordered substances such as polymers, 2D materials and bulk crystals, polarization-dependent experiments illuminate structural properties including anisotropy.

In this Technical Note, we illustrate the potential of polarization-resolved spectroscopy and imaging on samples from the fields of geology, polymers, biomineralization studies and 2D materials research.

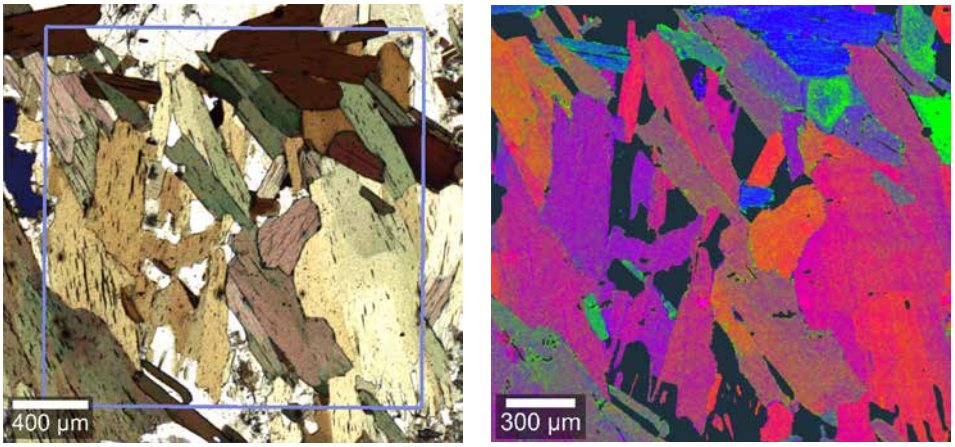

Figure 1: Parallel polarized white light transmission image (left panel) and Raman image made using TrueComponent Analysis (right panel) of a 25µm thin section of black mica revealing different crystal orientations.

Microscope setup with polarization control

All measurements presented here were performed with Oxford Instruments WITec Raman microscopes equipped with integrated polarization modules. For polarization-resolved white light imaging, two independent polarization filters were introduced to the optical beam path: the first (polarizer) is positioned behind the unpolarized white light source, the second (analyzer) after the sample in the detection beam path. For all laser-based polarization-resolved spectroscopic measurements including Raman spectroscopy, SHG and photoluminescence spectroscopy, dedicated polarizer and analyzer modules were used (Figure 2): Here, the polarizer consists of a freely rotatable half-wave plate that precisely orients the linearly polarized excitation beam's polarization on the sample. Optionally, a quarter wave plate can facilitate left- or right-handed circularly polarized light. The analyzer module in the detection beam path again allows for the selection of a specific linear polarization state of the scattered light to be studied. By rotating the analyzer, the directional emission pattern of a vibrational mode can be probed. Both polarizer and analyzer are independently rotatable in alpha300 systems, offering complete freedom in selecting polarization configurations. The optional motorization of the analyzer and polarizer modules enables the recording of automated polarization-dependent imaging series (see example abalone shell).

There is also the option of placing an additional λ/2 or λ/4 wave plate in the combined excitation and detection beam path. The λ/4 wave plate enables dedicated studies of the helicity of the scattered light, which is useful for investigating the sample's out-of-plane orientation [2].

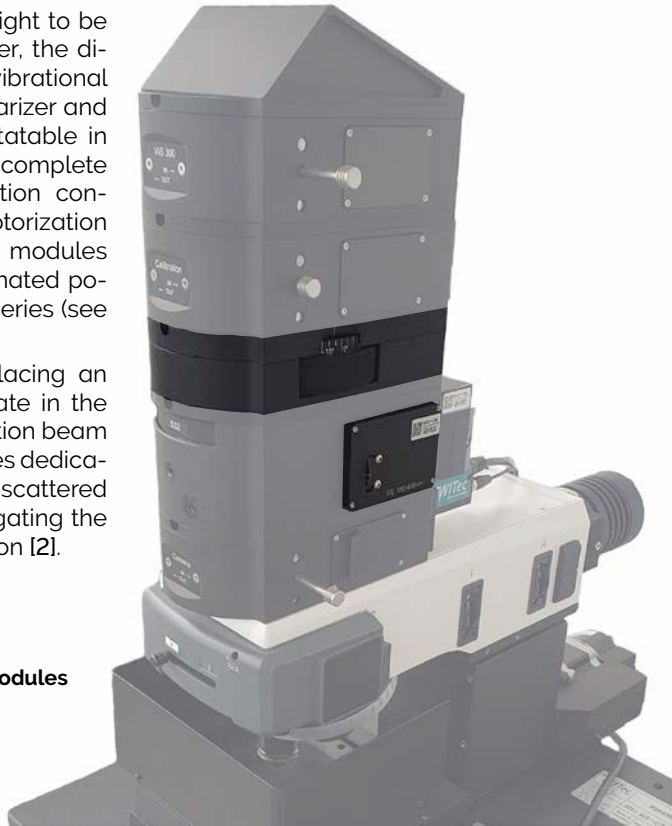

Figure 2: Polarizer and analyzer modules in a WITec alpha300 R system

WITec Wissenschaftliche Instrumente und Technologie GmbH
Lise-Meitner-Str. 6, D-89081 Ulm, Germany
Tel. +49 (0) 731 140 700, Fax +49 (0) 731 140 70200
info@WITec.de, https://raman.oxinst.com

Info Box: Polarization-resolved Raman spectroscopy

Raman spectroscopy that makes use of polarization effects relies on the electromagnetic nature of light, as polarization corresponds to the direction along which the electric field is oscillating. The wave equation (derived from Maxwell's equations) dictates that the magnetic and electric fields of the electromagnetic wave always oscillate perpendicular to its propagation direction. While unpolarized light is a superposition of waves with their electric fields oscillating in random directions, the electric fields of all waves are oriented in parallel for polarized light. Dependent on the molecular symmetry of the sample, the vibrational modes visible in the Raman spectra can be sensitive to the polarization angle of the excitation light. This reflects in a vibrational mode's Raman signal strength varying with the angle of polarization of the incident light, as visible in many in-plane anisotropic samples. At the same time, unoriented or isotropic crystal/molecular structures show no pronounced polarization dependence in their individual Raman peak intensities. Consequently, polarization-resolved Raman spectroscopy can provide much more profound information on the studied sample such as its structure and orientation of different domains.

Excitation path

Detection path

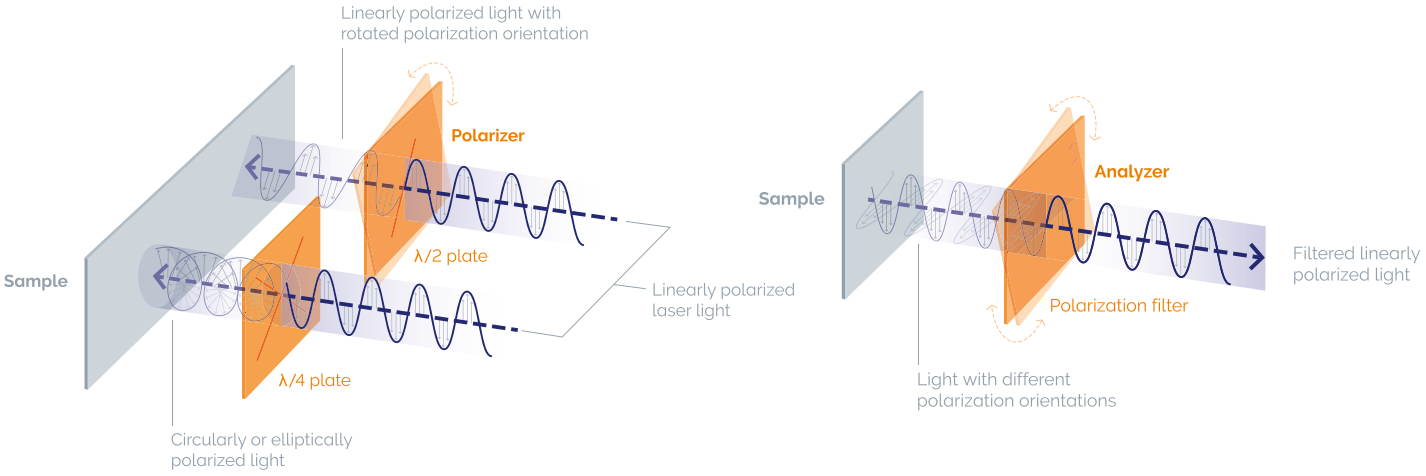

Figure 3: Schematic image of polarization control components.

Excitation path: The coherent, linearly polarized incident light is emitted from a laser with its electric field oscillating perpendicular to the propagation direction. The linear polarization state can be rotated to the desired orientation using a half-wave (λ/2) plate in the polarizer module. A quarter-wave (λ/4) plate may be introduced to produce elliptically or circularly polarized light.

Detection path: Using a polarization filter, i.e., the analyzer in the beam path before the detector, the polarization state of the detected light can be selected.

Visualizing the molecular processes in polyethylene stretching

Introduction

Polyethylene (PE) is a synthetic polymer with the chemical formula $(CH_2)_n$, which is one of the most commonly used materials for plastic packaging. Its molecular fiber structure and the possibility of introducing crosslinks between the fibers allow for the creation of plastics with different physical properties that are useful for a wide range of applications. Commercial PE products are sorted into two major groups: High-density PE (HDPE), including more rigid materials and those that appear more opaque, and low-density PE (LDPE), which provides high flexibility and is more transparent. As such, LDPE is commonly used as plastic wraps for food packaging to preserve and protect the food from chemical, biological and physical factors in the environment. In the following experiments, polarization-dependent Raman measurements were used to investigate the effects of plastic foil stretching on the molecular PE fiber orientation.

Experimental details

The experiments were carried out at Swiss Federal Laboratories for Materials Science and Technology (Empa). Automated polarization series were obtained over the full polarization rotation (360°) of the electric field of the laser light with one spectrum being recorded at every degree of rotation. A Linkam modular force stage (Linkam MF-stage) was used for the stress measurements of the polyethylene foil. Here, the material was stretched from 15 mm in its unstressed state up to 40 mm when fully stretched (Figure 4) and polarization series were obtained at 10, 15, 20 and 25 mm of stretching. All measurements were performed with a 532 nm excitation laser and a 50x/0.55 LWD objective.

A

B

Figure 4: Picture of the experimental setup.

PE sample fixed within the Linkam modular force stage under the Raman microscope. **(A)** Material unstretched (15 mm) **(B)** Material fully stretched (40 mm).

A

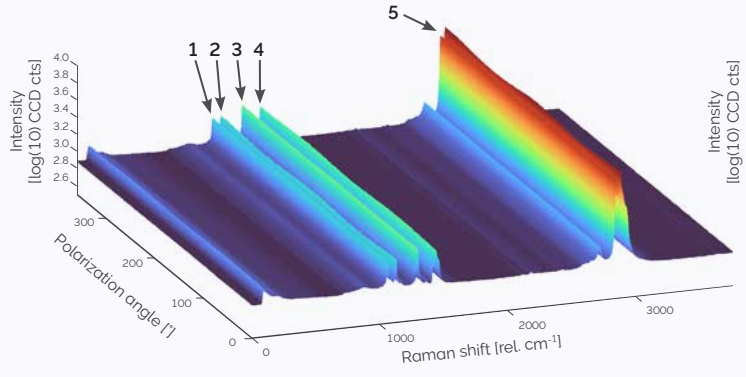

B

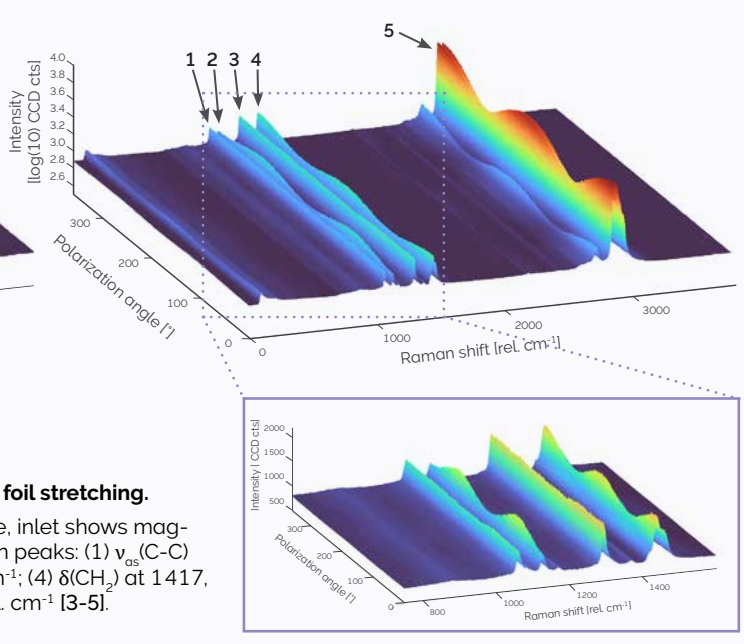

Figure 5: 3D heatmap of polarization-resolved Raman spectra in PE foil stretching.

(A) Unstretched polyethylene foil. **(B)** Fully stretched ($\Delta L/L_0$ = 5/3) state, inlet shows magnification of the fingerprint area (800 - 1600 rel. cm^{-1}). Labelled Raman peaks: (1) ν_{as}(C-C) at 1063 rel. cm^{-1}; (2) ν_s(C-C) at 1130 rel. cm^{-1}; (3) $\tau(CH_2)$ at 1297 rel. cm^{-1}; (4) $\delta(CH_2)$ at 1417, 1441 and 1464 rel. cm^{-1}; (5) $\nu_{as}(CH_2)$ and $\nu_s(CH_2)$ at 2849 and 2883 rel. cm^{-1} [3-5].

WITec Wissenschaftliche Instrumente und Technologie GmbH
Lise-Meitner-Str. 6, D-89081 Ulm, Germany
Tel. +49 (0) 731 140 700, Fax +49 (0) 731 140 70200
info@WITec.de, https://raman.oxinst.com

Results

The polarization-resolved analysis revealed a characteristic Raman spectral pattern for PE with five major peaks, which were independent of the polarisation direction of light in the unstretched material (Figure 5A). In contrast, the Raman modes for the symmetrical C-C stretching ν_s(C-C) (1130 rel. cm^{-1}), CH_2 bending $\delta(CH_2)$ (1417, 1441 and 1464 rel. cm^{-1}) and C-H stretching ν(C-H) (2849 and 2883 rel. cm^{-1}) showed polarization-dependent intensity changes in the fully stretched condition, while the asymmetrical C-C stretching mode (1063 rel. cm^{-1}) was still not affected (Figure 5B).

In the following, the ν_s(C-C) and the C-H stretching modes, both being polarization dependent but in opposite angular orientations, were investigated in more detail during the PE stretching process. For data evaluation, their spectra were normalized to the Raman band at 1063 rel. cm^{-1} of asymmetric C-C stretching, as no strong polarization dependence of the Raman signal was observed here in both the unstretched and stretched condition. The respective polar plots are shown in Figure 6.

In its relaxed state, the PE foil shows a homogenous Raman intensity for all polarization angles for both investigated spectral regions (Figure 6 – yellow color). This can be explained by an isotropic distribution of the fibers, exhibiting no predominant direction in the material. Stretching the foil with the Linkam MF-stage by 10 mm from its initial 15 mm (unstretched) to 25 mm ($\Delta L/L_0$ = 2/3) results in differences in the Raman signals with respect to the polarization of the incident light (Figure 6 – orange color). The C-C stretching shows intensity minima for 0° and 180° polarization angles and maxima at 90° and 270°. The intensity pattern of the CH-stretching mode follows the inverse orientations (maxima at 0° and 180° and minima at 90° and 270°, respectively). Stretching the foil even further by 25 mm ($\Delta L/L_0$ = 5/3) to a total length of 40 mm enhances these intensity differences between the polarization angles (Figure 6 – red, purple and blue).

Based on the obtained data and changing Raman intensities at different polarization angles, the orientation direction of the PE fibers within the plastic foil can be deduced. While molecular bonds parallel to the polarization direction of the laser light cause high Raman band intensities, decreased Raman signals are detected for perpendicular oriented bonds. Hence, for the investigated sample, the following interpretation can be made: the isotropic orientation of the PE fibers in unstretched condition is modified when applying a pulling force to the material. In the stretched condition, the PE fibers show a highly oriented (anisotropic) distribution, with the longitudinal axis of the fibers in line with the polarization of the laser light at 90° (Figure 7). The C-H stretching bonds align in the orthogonal orientation to this axis with increasing pulling force.

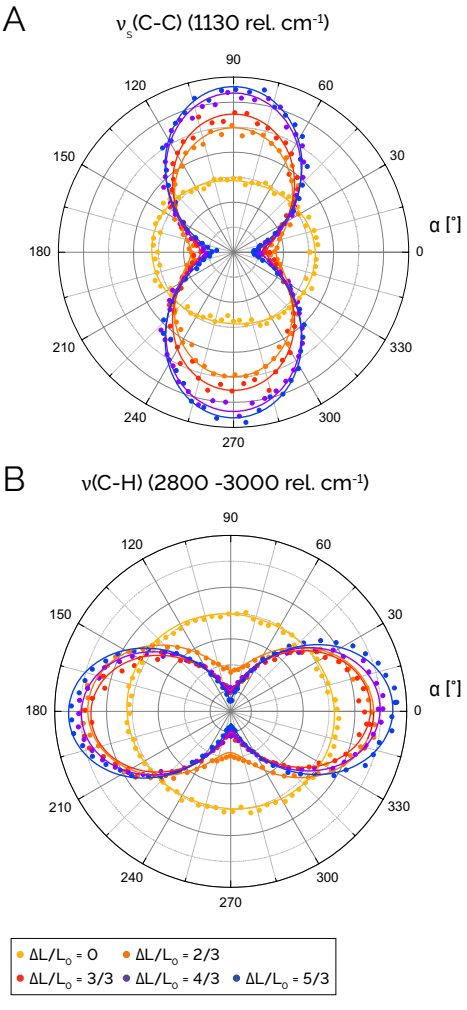

Figure 6: Polar plots of PE foil within stretching.

(A) Symmetrical C-C stretching band at 1130 rel. cm^{-1}. **(B)** C-H stretching region at 2800 - 3000 rel. cm^{-1}. The dots represent the experimental data, the line shows the fit. Stretching color coded from unstressed (yellow) to $\Delta L/L_0$ = 5/3 (blue).

Conclusion

The presented experiment is an example of how a materials' structural orientation can be determined using polarization-dependent Raman spectroscopy. As the polarization orientation of the incident laser light was a known factor in the measurements, the macroscopic PE fiber orientation in the plastic wrap was easily established. The method is especially useful for investigating the same sample in different conditions, such as the different measures of stretching shown here, due to its nondestructive nature and as it does not require additional sample preparation.

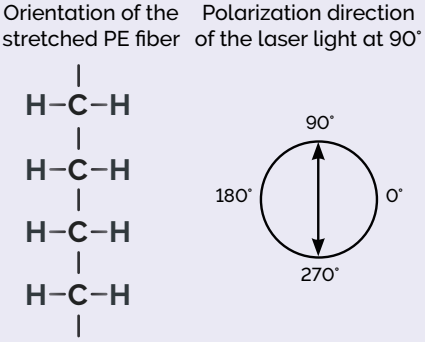

Figure 7: Scheme of the stretched PE fibers.

Orientation in relation to the polarization direction of the exciting light.

Polarization-resolved Raman spectroscopy of 2D materials

Introduction

Ever since the fabrication of monolayer graphene in 2004, the field of 2D materials research has been motivated by their intriguing optical, electronic, and mechanical properties. Recently, in-plane anisotropic 2D semiconductors have become subject of particular interest due to their properties being not only restricted in 2D, but also exhibiting an inherent in-plane directionality. Naturally, this young scientific field requires fast, high-resolution tools for material characterization. To this end, the benefits polarization-resolved Raman spectroscopy can provide for 2D materials research and engineering are illustrated in the following.

2D semiconductor MoO_3

Here, we focus on the in-plane anisotropic van-der Waals semiconductor molybdenum trioxide (α-MoO_3) with a direct electronic bandgap of ~3 eV (410 nm). MoO_3 exhibits an orthorhombic crystal structure (space group Pnma) with the lattice constants a = 0.396 nm, b = 1.382 nm, and c = 0.373 nm, where the van-der-Waals stacking direction is along [010] (Figure 8). The vdW layer consists of a double layer of distorted octahedra, wherein molybdenum and oxygen atoms are covalently bound. The in-plane anisotropy stems from the arrangement of three classes of oxygen atoms with different oxidation states: single-coordinated ($O^{(1)}$) along [010], double-coordinated ($O^{(2)}$) along [100], and tri-coordinated ($O^{(3)}$) along the [001] direction. The different Mo-O bonds along the crystallographic axes eventually give rise to a plethora of vibrational modes, many of which are Raman- or IR-active, with the latter supporting in-plane hyperbolic phonon polaritons [6].

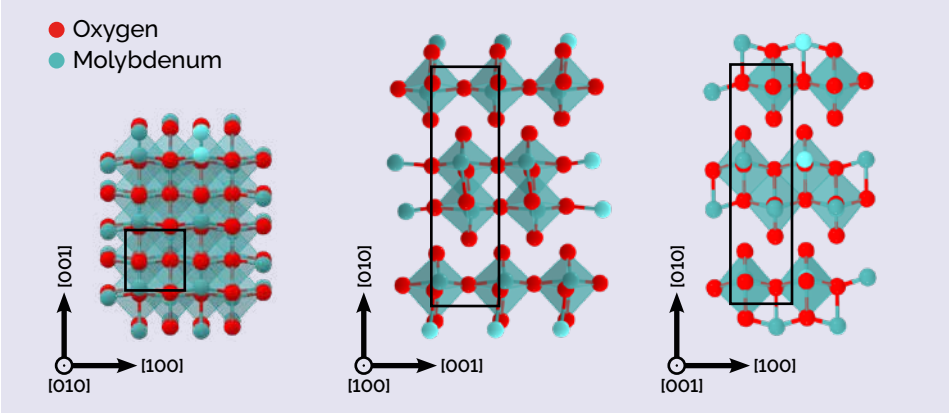

Figure 8: Crystal structure of α-MoO_3.

Crystal structure shown in three different orientations. Black box indicates the unit cell with the parameters: a = 0.396 nm, b = 1.382 nm, c= 0.373 nm.

Representation generated with Crystal Toolkit [7].

Experimental details

The investigated 25 × 4 µm² MoO_3 flake depicted in Figure 9 was exfoliated onto a SiO_2/Si substrate with the MoO_3 bulk crystal grown using the Bridgman technique. As the material typically breaks parallel to its in-plane crystallographic axes, the flakes come in a rectangular shape. The polarization geometry is illustrated in the inset (Figure 9). Here, the polarization angle α of incident light is defined against the microscope's x-axis with the analyzer in the detection beam path always parallel to the incident polarization direction. All measurements were performed using a 100x/0.9NA objective and 1.0 mW of power at 532 nm excitation wavelength.

Polarization-resolved Raman spectra

Raman spectra of the MoO_3 flake with incident and detected polarization parallel to the [100] (black) and [001] direction (red) are shown in Figure 10A: The Raman spectra reveal several sharp peaks in the 0 to 1100 rel. cm^{-1} range, many of which exhibit a pronounced polarization dependence. For instance, the Raman mode at the Raman shift of 160 rel. cm^{-1} (highlighted blue) has its maximum when excited along the [001] direction, whereas the Raman mode at 820 rel. cm^{-1} (yellow) shows the opposite behavior. Moreover, some Raman active modes are barely visible when excited parallel to an in-plane crystal axis, for instance at 284 and 667 rel. cm^{-1} (shaded red and green), which can be attributed to the nature of the vibrational mode. Note that the first and second order Si peaks stemming from the substrate are visible due to the finite thickness of the MoO_3 flake.

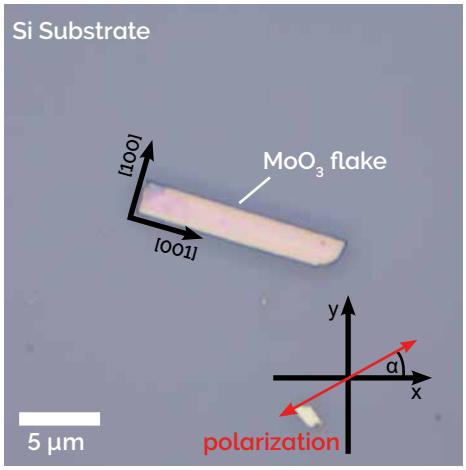

Figure 9: Optical image of MoO_3 sample.

Investigated 25 × 4 µm² MoO_3 flake with the in-plane crystal axes indicated. The inset depicts the layout of the polarization in the experiment.

WITec Wissenschaftliche Instrumente und Technologie GmbH
Lise-Meitner-Str. 6, D-89081 Ulm, Germany
Tel. +49 (0) 731 140 700, Fax +49 (0) 731 140 70200
info@WITec.de, https://raman.oxinst.com

Polarization-resolved Raman intensities

In order to obtain additional information about the four selected modes, a measurement series was performed in which the angle of incident polarization **α** together with the analyzer was rotated from 0° to 360° and a spectrum recorded every 5°. This measurement layout consisting of a stationary sample and controlled polarization is particularly advantageous for 2D material investigations as the position of the excitation on the sample doesn't change, allowing for automated measurements (the presented series took 2.5 minutes to record). The results for the four modes are displayed in Figure 10B in individual polar plots, with the respective integrated Raman intensity on the r-axis. Here, the experimental data are represented by the data points and the black curves correspond to fits according to **[8]**.

- *A_g-mode at 160 rel. cm^{-1}*:
Two-lobed mode with its maxima oriented parallel to the [001] direction.
- *B_{2g}-mode at 284 rel. cm^{-1}*:
Four-lobed mode with its maxima 45° off-axis.
- *B_{2g}, B_{3g}-mode at 667 rel. cm^{-1}*:
Four-lobed mode with its maxima 45° off-axis.
- *A_g, B_{1g} -mode at 820 rel. cm^{-1}*:
Two-lobed mode with its maxima oriented parallel to the [100] direction (A_g component) superposed by a weaker four-lobed shape that has its maxima along the main crystal axes (B_{1g} component).

Overall, the fits nicely match the data and the shapes of the modes correspond with data found in literature **[9]**.

Conclusion

Using the example of molybdenum trioxide, we demonstrated the great potential polarization-resolved Raman spectroscopy offers to the field of 2D materials: fast, nondestructive assignment of crystallographic axes and determination of the type of vibrational modes. This is in addition to the standard properties accessible with Raman spectroscopy, such as information about crystal quality, stress/strain and material composition.

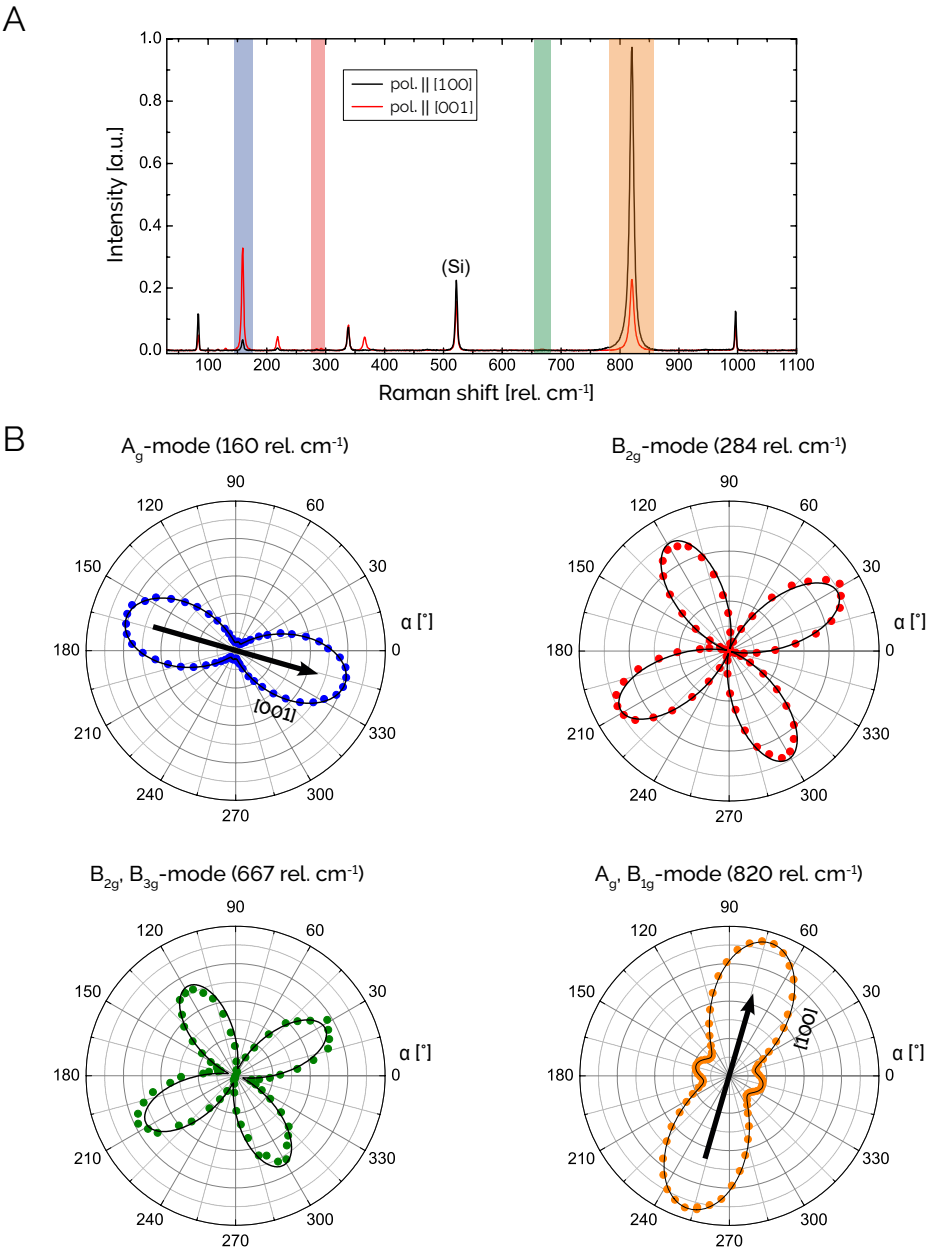

Figure 10: Polarization-dependent Raman spectra of MoO_3.
(A) Raman spectra of MoO_3 with both incident and detected polarization along the [100] (black) and [001] directions (red). **(B)** Integrated Raman intensity of different vibrational modes as a function of angle of polarization **α**. The polar plots represent the experimental data (datapoints) and their corresponding fits (black lines).

Polarization-dependent Raman imaging of an abalone shell

Introduction

In the search for materials with great stiffness, strength, and toughness, mollusk shells serve as a source of inspiration for the design of advanced functional materials [10]. Over the years biominerals have been refined by natural selection, leading to the unique forms and functions we observe today. For studying their exceptional structure, polarization-resolved Raman imaging is a powerful tool that can reveal biomineral composition and crystal orientation.

Abalone (*Haliotis rufescens*) shell

An abalone shell consists of polymorphs of $CaCO_3$ [11]. The outer part of the shell is formed of calcite with a trigonal R3c crystal form. The translucent inner part called nacre is built up from platelets of aragonite. The orthorhombic crystal structure of aragonite with a unit cell (Pnma space group) with the lattice constants: a = 0.495 nm, b = 0.796 nm and c = 0.573 nm is shown in Figure 11.

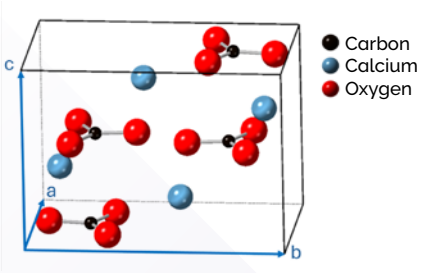

Figure 11: Crystal structure of aragonite.
Unit cell (black box) with the dimensions a = 0.495 nm, b = 0.796 nm and c= 0.573 nm.

Sample preparation

Samples were cut from an abalone shell (*Haliotis rufescens*) using a diamond saw. Nacre samples (~ 20 × 5 × 5 mm^3) were embedded in epoxy resin with the c-axis parallel to the surface and manually polished in dry conditions with a series of SiC sandpapers of decreasing grain size to reach a surface roughness of a few hundred nanometers.

RISE measurements on nacre

In this study, correlative Raman and SEM imaging was used to examine the aragonite phase of the nacre, where the platelets form a brick-and-mortar structure perpendicular to the growth direction (Figure 12A).

Imaging was performed with a Raman Imaging and Scanning Electron (RISE) Microscope in low vacuum mode at 15 Pa and an acceleration voltage of 15 kV. Raman data were collected from an area of 20 x 15 μm^2 (100 x 75 Raman spectra, 0.2 s integration time per spectrum), using a 532 nm excitation laser at 10 mW. For the polarization-dependent Raman measurements, the incident laser light was oriented in the growth direction of the aragonite platelets (horizontal direction in Figure 12A). On the detection side, all of the Raman scattered light was collected.

The Raman spectra acquired from the nacre show a characteristic pattern for aragonite (Figure 12B). Raman bands at low wavenumbers originate from the CO_3 lattice vibration modes such as the translational mode and wobbling (153 rel. cm^{-1} and 206 rel. cm^{-1}, respectively). The strong peak at 1085 rel. cm^{-1} corresponds to CO_3 stretching [12]. When the acquired Raman image is overlaid onto the SEM image (Figure 12C) the platelet's co-orientation along the growth direction is revealed. This corresponds to the c-direction in the schematic in Figure 11.

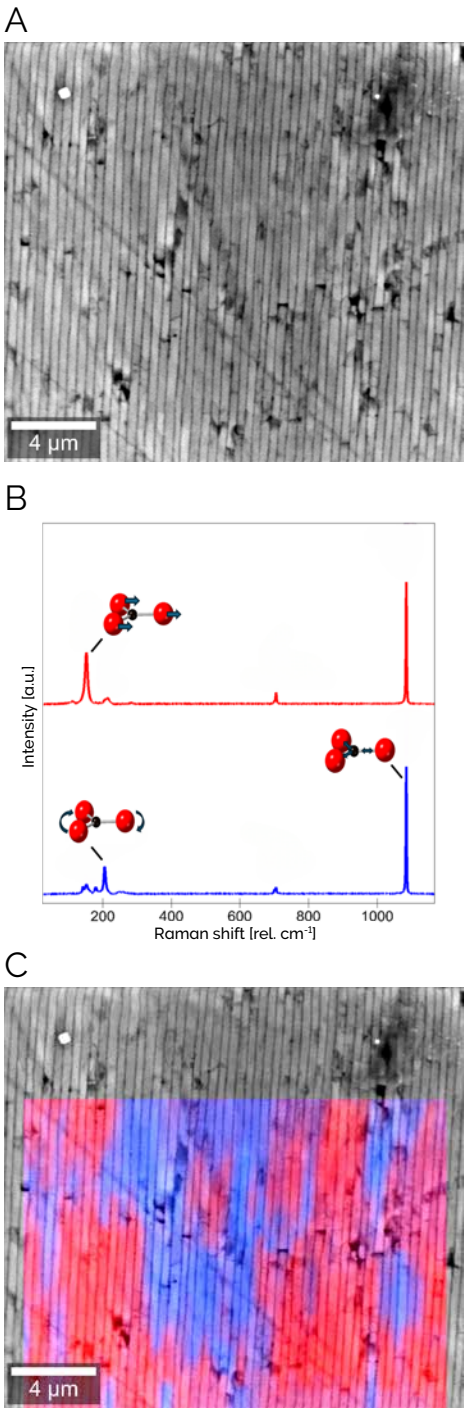

Figure 12: RISE microscopy of nacre.
(A) SEM image of nacre. **(B)** Two distinct Raman spectra of aragonite of different crystal co-orientations (red and blue) with characteristic peaks for the translational (153 rel. cm^{-1}), wobbling (206 rel. cm^{-1}) and CO-stretching (1085 rel. cm^{-1}) modes. **(C)** Overlaid Raman and SEM image. The color code corresponds to the colors of the spectra in (B).

WITec Wissenschaftliche Instrumente und Technologie GmbH
Lise-Meitner-Str. 6, D-89081 Ulm, Germany
Tel. +49 (0) 731 140 700, Fax +49 (0) 731 140 70200
info@WITec.de, https://raman.oxinst.com

Automated polarization-resolved Raman imaging

In the next step, a series of Raman images of the nacre with rotating polarization (5 degrees per step) was recorded while maintaining a constant perpendicular cross-orientation of the incident and detection angles (Figure 13). Each of the 20 presented images in Figure 13 was acquired from an area of 40 x 40 µm² (160 x 160 Raman spectra, integration time per spectrum 0.06 s). In the initial state, the polarization of the incident light was parallel to the c-axis of the aragonite crystal (Figure 13, 0 degrees). The TrueComponent Analysis of the data processing software was used to evaluate the 160 x 160 Raman spectra for 37 angular directions simultaneously (a total of 947,200 Raman spectra) and identified three different components (Figure 13). The red and blue areas represent the co-oriented structures similar to Figure 12C. Both show a strong polarization dependence. Variations in C-O stretching are apparent with the green spectral component, which exhibits polarization effects opposite in angle from the blue and red components.

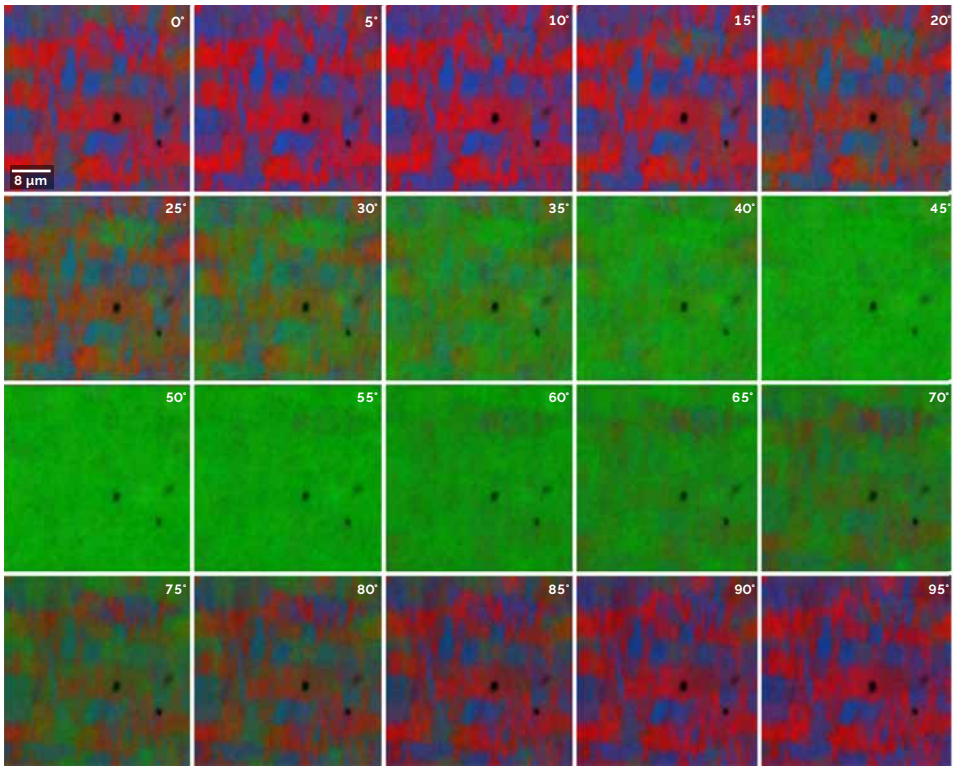

Figure 13: Polarization-dependent Raman imaging of nacre.

Color-coded Raman images of nacre acquired at different polarization angles. Angle 0 degrees reflects polarization perpendicularto the c-axis of the abalone nacre.

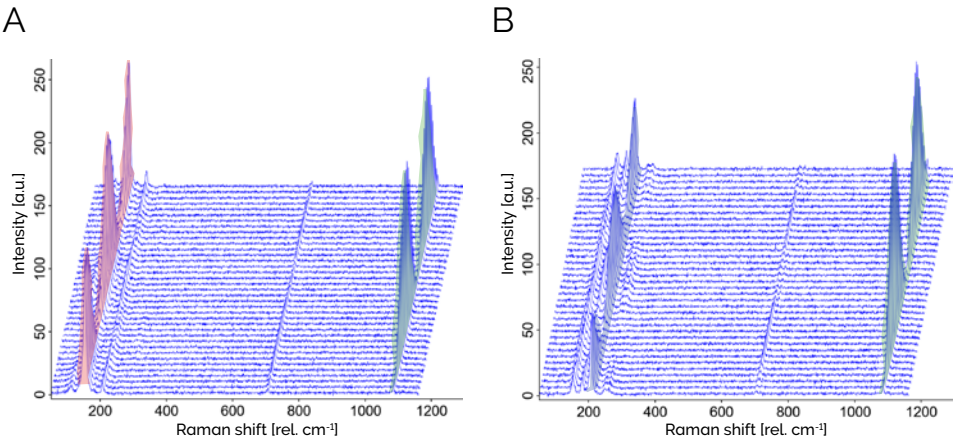

Figure 14: Polarization-dependent Raman spectral changes in nacre.

Waterfall plots of polarization-dependent Raman spectra in nacre. Individual spectra are given for 37 different polarization angles (5 degree steps). The spectral information is given for two individual positions representative for red **(A)** and blue **(B)** colored areas of Figure 13. The coloration in the plots highlights the characteristic spectral features found in these areas.

The underlying changes in the Raman band intensities as a function of the polarization angle are illustrated for two sample positions for the entire series of 37 angles in waterfall plots (Figure 14). These representations of the Raman spectra clearly show that lattice vibrations of nacre are extinguished when the polarization changes from 0 degrees (perpendicular to the c-axis) to 45 degrees. At the same time, the intensity of the C-O stretching band reaches its maximum at this polarization angle.

Conclusion

Using the example of nacre, we demonstrated the immense potential polarization-resolved Raman ima-ging offers for obtaining a better understanding of the crystal structures in biominerals. It is a fast, nondestructive imaging technique, particularly suitable for revealing information about crystal orientation, unit cell distribution and material composition.

Polarized White Light and Raman Microscopy on Biotite

Introduction

Since the invention of polarizers by William Nicol in 1829 and the development of the first polarizing microscope by Giovanni Battista Amici in 1830 [13,14], geosciences and mineralogy have been revolutionized by the ability to analyze rock thin sections between a set of two polarizers with white light illumination. Through the rotation of the two polarizers relative to each other and to the orientation of individual mineral grains, the resulting optical effects allow conclusions to be made about materials' physical properties. Additional polarization-resolved Raman spectroscopy measurements provide detailed insight on the crystallographic orientations in the rock. In this investigation we combine both methods and semiquantitative approaches to identify two different formation stages of the mineral biotite based on its geometrical alignment in the sample.

Sample

To differentiate geometrically hetero-geneous biotite alignments, a sample was chosen in which the relationship between two formation processes (metamorphic crystal alignment vs. magmatic melt penetration) is not obvious from the cross-cutting relationship. Figure 15 shows this situation in a stitched white light image of a 40 x 20 mm thin section from the abandoned Griffins Find Gold Mine, Western Australia. Two rock-forming generations could be assumed, as the metamorphic layering fabric of a µm-sized mafic granulite (yellow region: biotite-feldspar-pyroxene) is intersected by a vein of mm-sized mineral grains with different mineralogical paragenesis (red region: quartz-feldspar-biotite-pyroxene). However, it can also be seen that this vein propagates along the lineation and fabric of the metamorphic orientation. This raises the question of whether this difference already existed (e.g. due to irregularities in the parent rock) or a possible melt penetration and recrystallization of the rocks occurred along the pre-developed lineation.

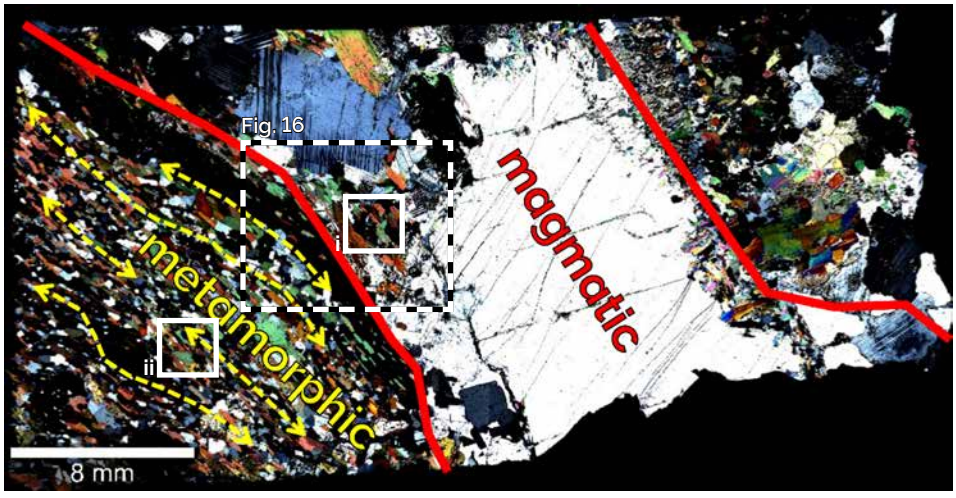

Figure 15: Overview white light image of metamorphic rock with magmatic domain.

Cross-polarization illumination showing a magmatic vein (red) crosscutting a metamorphic rock along its pre-developed metamorphic fabric (yellow). White rectangles (**i** and **ii**) represent the selected areas for the following measurements; position of Figure 16 indicated with box.

A potential explanation for the sample's structure is that single crystals in a metamorphic rock were aligned perpendicular to the direction of pressure over millions of years and then suddenly the rock was fractured and underwent emplacement by melt of magmatic origin. Support for this hypothesis could be found in detecting highly aligned biotite in the metamorphic areas (pressure-induced solid reactions and deformation), while seeing the full degree of freedom for arbitrary biotite crystallization (cavitation and crystallization from a liquid) in the magmatic areas.

Polarized white light microscopy investigation of biotite crystals

With polarized white light microscopy, optical properties of materials can be visualized to aid in characterizing their composition and structure. The underlying effect – birefringence – is specific for individual materials and is caused by the anisotropism in the crystal lattice, splitting of the polarized light into two beam paths, and different propagation speeds of the electromagnetic waves along different crystal planes. This creates a characteristic phase shift between both waves, which can be represented as interference colors.

Here we show a 25 µm thin rock section in different illumination setups: reflected light (Figure 16A), transmitted light (Figure 16B), transmitted light in parallel polarization (parallel-oriented polarizer and analyzer, ||Pol, Figure 16C) and cross polarization (orthogonal orientation of polarizer and analyzer, xPol, Figure 16D). While reflected and unpolarized transmitted light images (Figures 16A and 16B) show the presence of opaque (ore minerals) and transparent crystals (major rock forming minerals), the coloring visible in the ||Pol illuminated setting (Figure 16C) displays their intrinsic colors and, most importantly, their morphology and formative relationship. The interference colors in the xPol configuration (Figure 16D) indicate which minerals are present and reflect qualitative differences in the crystallographic orientation of their crystal lattices. In combination, the four images reveal mineral phase identities as well as processes of rock formation by connecting optical properties to crystallographic orientations and other crystal properties (i.e. crystal fabrics: habits, cleavages, twinning, inclusions, exsolutions, deformations).

WITec Wissenschaftliche Instrumente und Technologie GmbH
Lise-Meitner-Str. 6, D-89081 Ulm, Germany
Tel. +49 (0) 731 140 700, Fax +49 (0) 731 140 70200
info@WITec.de, https://raman.oxinst.com

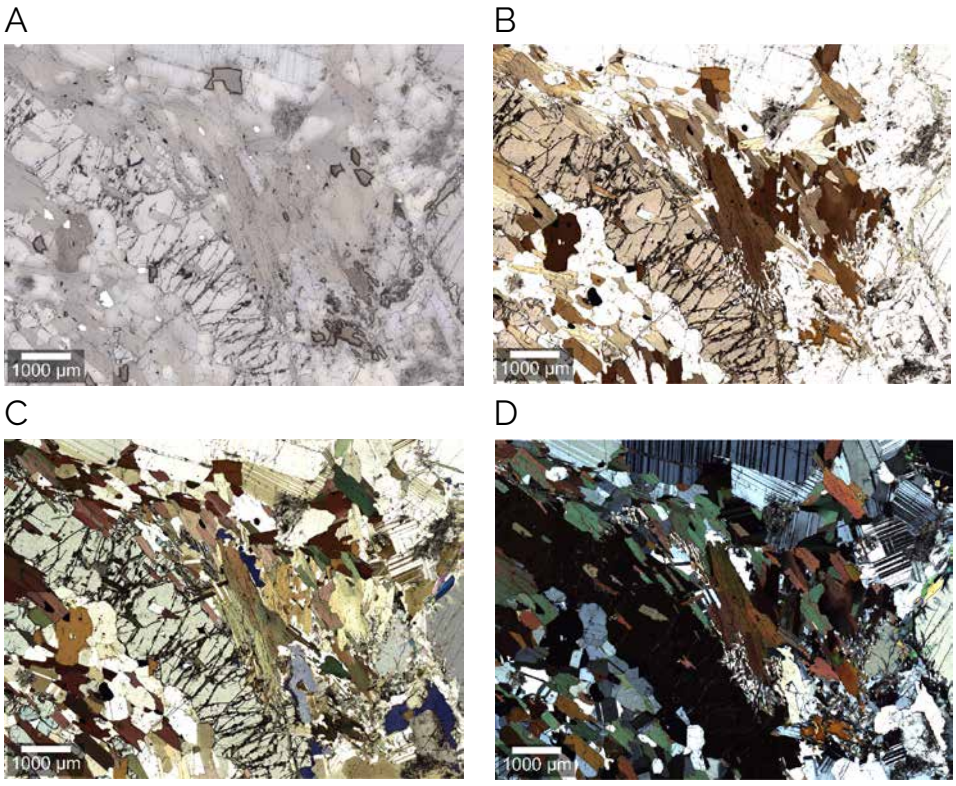

Figure 16: White light images of biotite mineral acquired using different illumination techniques.

Reflected **(A)** and transmitted **(B)** light image. Transmitted light image at parallel polarization (||Pol) **(C)** and 90° crossed polarization setup (xPol) **(D)**. Area section given in Figure 15.

Polarization-resolved Raman spectroscopy of biotite

Raman spectroscopy was employed to test our hypothesis on the origin of two biotite generations in the rock. The first approach was a statistical investigation of two areas in the sample (respectively Figure 15: white squares) that recorded fully automated 360° polarizer series on 15 randomly selected biotite crystals in both areas. A 50x/0.8NA objective and a 532 nm excitation laser at 10 mW were used. A series of single spectra was acquired at an integration time of 0.5 s per spectrum and 10 accumulations with a polarizer angle step size of 5° through a full rotation. Two selected Raman modes of biotite and schematic representations of their respective vibrations in the crystal structure are given in Figure 17. Both the νTO_4 stretching mode (T-O stretch of SiO_4- and AlO_4-tetrahedron movements along the c-axis, green vectors) and the δT_6O_6 ring modes (O3-T-O1 and T-O2-T bend in the T_6O_6-ring adjacent to the cleavage planes, blue vectors) were pre-evaluated to be unaffected by birefringence effects (Figure 17B) [15,16]. ▶

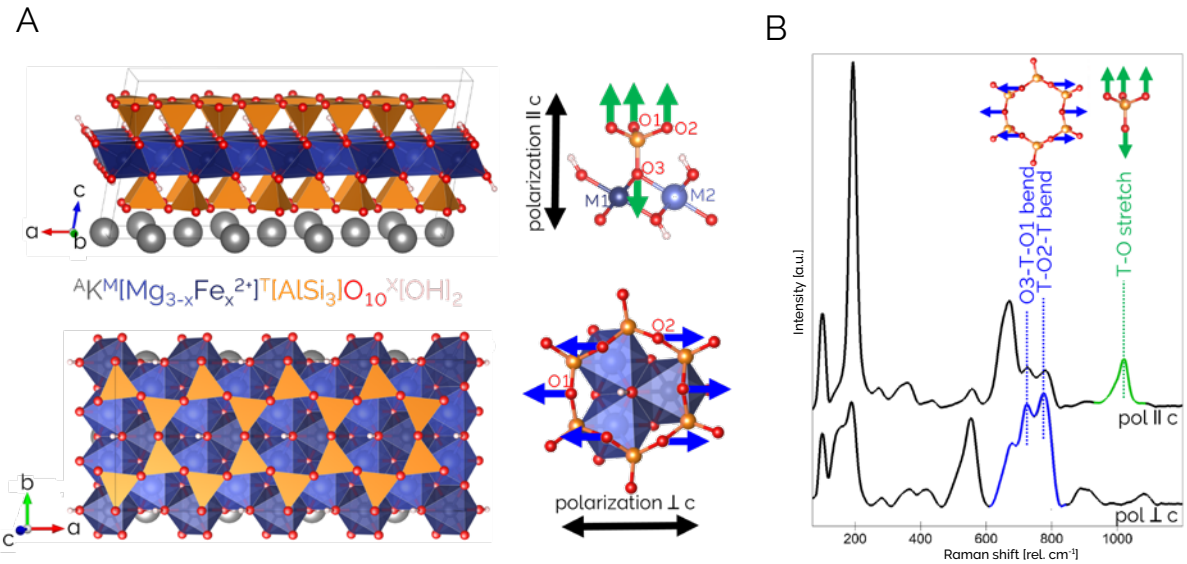

Figure 17: Structural formula, crystallographic models and polarization-resolved Raman spectra of biotite.

(A) Crystallographic models parallel to the b- and c-axis and structural formula of biotite. Coupling relationships are given for polarization orientations parallel and orthogonal to the c-axis. **(B)** Resulting polarization-dependent Raman spectra which exaggerate T-O stretch parallel to c-axis (SiO_4- and AlO_4-tetrahedron) and O3-T-O1 and T-O2-T bend orthogolal to c-axis (T_6O_6-ring).

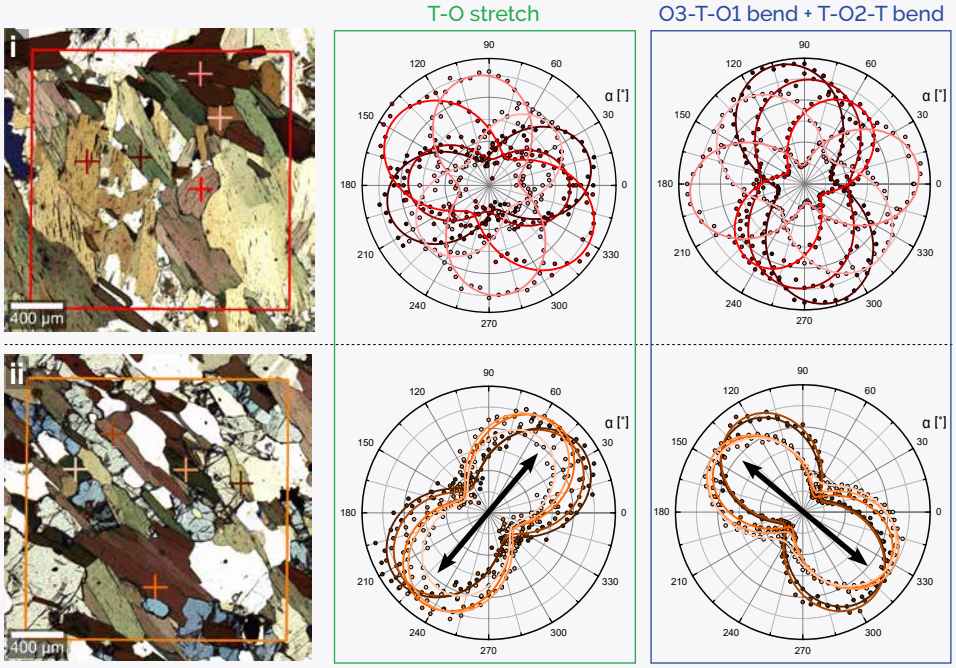

Figure 18: Polar plots of the biotite crystal orientations.

Measurement points and polar orientation plots of 5/15 polarizer series from the magmatic **(i)** and metamorphic region **(ii)**.

◀ For evaluation, polar orientation plots were extracted displaying the Raman band intensities of the νTO_4 stretching mode (green) and δT_6O_6 ring modes (blue) (Figure 18, 5 positions per area plotted). In the metamorphic part (ii) a clear orientation of the TO_4-tetrahedrons' T-O stretching mode along the 45° and 225° polarizer rotation and thus parallel to the former maximum pressure-induced stress regime can be observed. The O3-T-O1 and T-O2-T bending vibrations of the T_6O_6-rings, which correspond to the anisotropy of the crystal lattice and the preferred orientation of the layered structure of the biotite parallel to the (001) surface, are statistically regulated along the 135° and 315° polarization. In the magmatic part (i), however, the crystal axes are irregularly oriented in all spatial directions.

TrueComponent Analysis of biotite in Raman images

In a second approach, high-resolution confocal Raman images were acquired from the magmatic (i) and metamorphic (ii) areas and analyzed using the WITec TrueComponent Analysis data evaluation module. The images were recorded in a 2000 x 2000 µm² area at 0.1 s integration time per spectrum using a 50x/0.8 NA objective and a 532 nm excitation laser at 40 mW. In this analysis setup, only biotite spectra were included and three orientation endmembers (blue, green and red; Figure 19A: selected endmember crystals, Figure 19D: endmember Raman spectra) were pre-defined as internal standards for the crystallographic orientations. Their allocation was based on a detailed evaluation of the phase identification and by the determination of their crystallographic axis orientation in xPol illumination.

As a result, the TrueComponent Analysis algorithm created intensity distribution images (Figure 19B) in which the coloring of individual grains represents their orientation match with the pre-defined endmember orientations. The color palettes (inverse pole figures: red, blue and green) therefore correspond to spatial orientations in which the excitation laser is aligned perpendicular to the biotite (100), (010) and (001) sectional planes and the laser polarization is aligned in parallel with the crystallographic c-, a- and b-axes, respectively (Figure 19C).

The colors in the magmatically formed area (i) are close to the extremes of the color scale, indicating arbitrary biotite orientations in this section that originate from random crystallization in a melt phase. In contrast, the image of metamorphically regulated biotites (ii) shows a more uniform color spectrum, pointing to a similar orientation of all biotites in this area having been caused by high pressures applied over a long period of time.

In combination with the statistical Raman spectroscopic approach, these results confirm a difference in the two parts of the thin section with highly ordered biotite crystals in the metamorphic and irregular orientations in the melt emplacement areas, supporting the hypothesized manner of formation.

Conclusion

This study presented polarized white light and polarization-resolved Raman microscopy as effective methods for investigating biotite crystals and their crystallographic orientation. Using semi-quantitative approaches, the data supported the hypothesis of different crystallization stages in the rock formation. This clearly demonstrates the benefits of both techniques for characterizing geoscience samples.

WITec Wissenschaftliche Instrumente und Technologie GmbH
Lise-Meitner-Str. 6, D-89081 Ulm, Germany
Tel. +49 (0) 731 140 700, Fax +49 (0) 731 140 70200
info@WITec.de, https://raman.oxinst.com

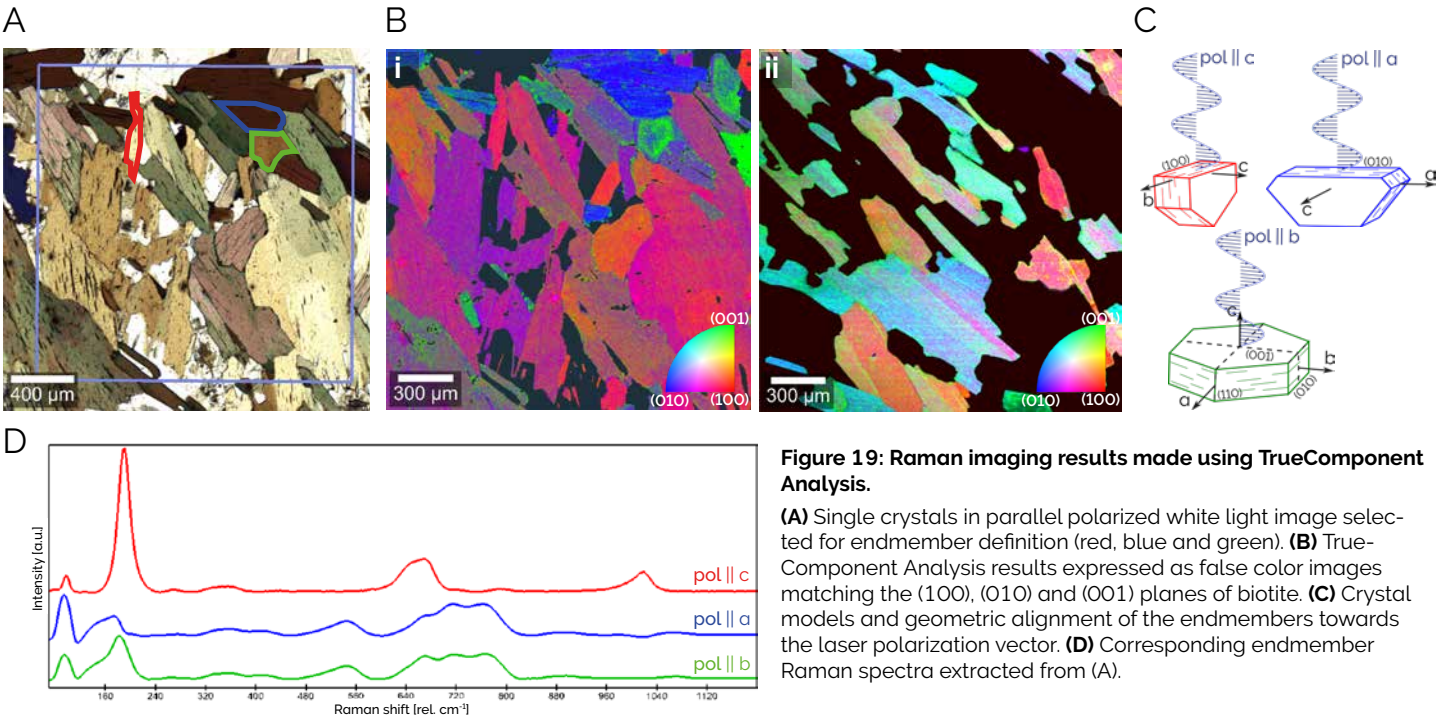

Figure 19: Raman imaging results made using TrueComponent Analysis.

(A) Single crystals in parallel polarized white light image selected for endmember definition (red, blue and green). **(B)** True-Component Analysis results expressed as false color images matching the (100), (010) and (001) planes of biotite. **(C)** Crystal models and geometric alignment of the endmembers towards the laser polarization vector. **(D)** Corresponding endmember Raman spectra extracted from (A).

References

[1] WITec Application Note "Correlative Imaging of MoS_2" https://raman.oxinst.com/assets/uploads/raman/materials/WITec-AppNote-MoS2-correlativeImaging.pdf

[2] Xu, B., Mao, N., Zhao, Y., Tong, L., & Zhang, J. (2021). Polarized Raman spectroscopy for determining crystallographic orientation of low-dimensional materials. *The Journal of Physical Chemistry Letters*, 12(31), 7442-7452.

[3] Allen, V., Kalivas, J. H., & Rodriguez, R. G. (1999). Post-consumer plastic identification using Raman spectroscopy. *Applied spectroscopy*, 53(6), 672-681.

[4] J. Fischer, G. M. Wallner, A. Pieber, (2008, May). Spectroscopical investigation of ski base materials. *Macromolecular symposia*, 2008, 265(1) p28-36. DOI: 10.1002/masy.200850504.

[5] Silva, D. J. D., & Wiebeck, H. (2019). Predicting LDPE/HDPE blend composition by CARS-PLS regression and confocal Raman spectroscopy. *Polímeros*, 29, e2019010. DOI: 10.1590/0104-1428.00218.

[6] de Oliveira, T. V., Nörenberg, T., ÁlvarezPérez, G., Wehmeier, L., TaboadaGutiérrez, J., Obst, M., ... & Eng, L. M. (2021). Nanoscale-Confined Terahertz Polaritons in a van Der Waals Crystal. *Advanced Materials*, 33(2), 2005777. DOI: 10.1002/adma.202005777.

[7] next-gen.materialsproject.org/toolkit

[8] Zheng, B., Wang, Z., Chen, Y., Zhang, W., & Li, X. (2018). Centimeter-sized 2D -MoO3 single crystal: growth, Raman anisotropy, and optoelectronic properties. *2D Materials*, 5(4), 045011. DOI: 10.1088/2053-1583/aad2ba.

[9] Seguin, L., Figlarz, M., Cavagnat, R., & Lassègues, J. C. (1995). Infrared and Raman spectra of MoO3 molybdenum trioxides and MoO3· xH2O molybdenum trioxide hydrates. *Spectrochimica Acta Part A: Molecular and Biomolecular Spectroscopy*, 51(8), 1323-1344. DOI: 10.1016/0584-8539(94)00247-9.

[10] Loh, H. C., Divoux, T., Gludovatz, B., Gilbert, P. U., Ritchie, R. O., Ulm, F. J., & Masic, A. (2020). Nacre toughening due to cooperative plastic deformation of stacks of co-oriented aragonite platelets. *Communications Materials*, 1(1), 77. DOI: 10.1038/s43246-020-00078-y.

[11] Lin, A. Y. M., Chen, P. Y., & Meyers, M. A. (2008). The growth of nacre in the abalone shell. *Acta Biomaterialia*, 4(1), 131-138. DOI: 10.1016/j.actbio.2007.05.005

[12] Farfan, G. A., Zhou, C., Valley, J. W., & Orland, I. J. (2021). Coupling mineralogy and oxygen isotopes to seasonal environmental shifts recorded in modern freshwater pearl nacre from Kentucky Lake. *Geochemistry, Geophysics, Geosystems*, 22(12), e2021GC009995. DOI: 10.1029/2021GC009995

[13] Nicol, W. (1829). On a method of so far increasing the divergency of the two rays in calcareous-spar, that only one image may be seen at a time. *Edinburgh new philosophical journal*, 6, 83-84.

[14] Amici, G. B. (1844). Note sur un appareil de polarisation. *Ann. Chim. Phys*, 12, 114-120

[15] McKeown, D. A., Bell, M. I., & Etz, E. S. (1999). Raman spectra and vibrational analysis of the trioctahedral mica phlogopite. *American Mineralogist*, 84(5-6), 970-976. DOI: 10.2138/am-1999-5-634.

[16] Aspiotis, S., Schlüter, J., Redhammer, G. J., & Mihailova, B. (2022). Non-destructive determination of the biotite crystal chemistry using Raman spectroscopy: how far we can go?. *European Journal of Mineralogy*, 34(6), 573-590. DOI: 10.5194/ejm-34-573-2022

WITec Microscopes

alpha300 S:
Scanning Near-field Optical Microscope

alpha300 A:
Atomic Force Microscope

alpha300 R:
Confocal Raman Microscope

alpha300 R*i*:
Inverted Confocal Raman Microscope

RISE®: Raman Imaging and Scanning Electron Microscope

alpha300 *apyron*™: Automated Confocal Raman Microscope

alpha300 *access*:
Confocal Micro-Raman System

Find your regional WITec and Oxford Instruments contact at https://raman.oxinst.com/contact

WITec Headquarters
WITec Wissenschaftliche Instrumente und Technologie GmbH
Lise-Meitner-Str. 6, D-89081 Ulm, Germany
Phone +49 (0) 731 140 700, Fax +49 (0) 731 14070 200
info@witec.de, https://raman.oxinst.com